The Astrophysical Journal, 865:131 (15pp), 2018 October 1 https://doi.org/10.3847/1538-4357/aadcf6

High-resolution ALMA Study of the Proto-brown-dwarf Candidate L328-IRS

Chang Won Lee[1,2], Gwanjeong Kim[1,2,3], Philip C. Myers[4], Masao Saito[5], Shinyoung Kim[1,2], Woojin Kwon[1,2],
A-Ran Lyo[1], Archana Soam[1], and Mi-Ryang Kim[1]

[1] Korea Astronomy & Space Science Institute, 776 Daedeokdae-ro, Yuseong-gu, Daejeon, Republic of Korea; cwl@kasi.re.kr
[2] Korea University of Science & Technology, 217 Gajungro, Yuseong-gu, Daejeon, 305-333, Republic of Korea
[3] Nobeyama Radio Observatory, National Astronomical Observatory of Japan, National Institutes of Natural Sciences, Nobeyama, Minami- maki, Minamisaku, Nagano 384-1305, Japan
[4] Harvard-Smithsonian Center for Astrophysics, 60 Garden Street, Cambridge, MA 02138, USA
[5] National Astronomical Observatory of Japan, National Institutes of Natural Sciences, 2-21-1 Osawa, Mitaka, Tokyo 181-8588, Japan

Received 2018 June 18; revised 2018 August 21; accepted 2018 August 22; published 2018 October 1

Abstract

This paper presents our observational attempts to precisely measure the central mass of a proto-brown dwarf candidate, L328-IRS, in order to investigate whether L328-IRS is in the substellar mass regime. Observations were made for the central region of L328-IRS with the dust continuum and CO isotopologue line emission at Atacama Large Millimeter/submillimeter Array (ALMA) band 6, discovering the detailed outflow activities and a deconvolved disk structure of a size of ∼87 × 37 au. We investigated the rotational velocities as a function of the disk radius, finding that its motions between 130 and 60 au are partially fitted with a Keplerian orbit by a stellar object of $\sim 0.30\,M_\odot$, while the motions within 60 au do not follow any Keplerian orbit at all. This makes it difficult to lead a reliable estimation of the mass of L328-IRS. Nonetheless, our ALMA observations were useful enough to well constrain the inclination angle of the outflow cavity of L328-IRS as ∼66°, enabling us to better determine the mass accretion rate of $\sim 8.9 \times 10^{-7}\,M_\odot\,\mathrm{yr}^{-1}$. From assumptions that the internal luminosity of L328-IRS is mostly due to this mass accretion process in the disk, or that L328-IRS has mostly accumulated the mass through this constant accretion rate during its outflow activity, its mass was estimated to be ~ 0.012–$0.023\,M_\odot$, suggesting L328-IRS to be a substellar object. However, we leave our identification of L328-IRS as a proto-brown dwarf to be tentative because of various uncertainties, especially regarding the mass accretion rate.

Key words: brown dwarfs – ISM: individual objects (L328, L328-IRS) – stars: low-mass

1. Introduction

The formation of brown dwarfs (BDs) is not yet well understood and still under strong debate. There are many suggestions as to how objects acquire the BD mass, including turbulent or gravitational fragmentation in a molecular cloud, like the case of low-mass star formation (Padoan & Nordlund 2004; Bonnell et al. 2008; Bate 2012), ejections of substellar objects from multiple star-forming regions or massive circumstellar disks (Boss 2001; Reipurth & Clarke 2001; Bate 2009; Basu & Vorobyov 2012), tidal shear and high-velocity dispersion present in a stellar cluster (Bonnell et al. 2008), and photo-erosion of a prestellar core by a nearby OB star (Whitworth & Zinnecker 2004). The underlying principle in these mechanisms is mostly related to the premature termination of accreting processes toward the point sources (see Luhman 2012; Lee et al. 2013).

The problem here is that such formation scenarios are mostly theoretical and have hardly been tested. Various observations on the early precursors of BDs like the proto-BDs containing the initial conditions of the BD formation will be essential for unraveling the mystery of BD formation.

In practice, however, identifying a bona fide proto-BD is very difficult. For this work we need to know the envelope mass, the mass accretion rate, and the central mass of the candidate. The envelope mass is important as it determines a mass to supply to the central source. The mass accretion rate is needed to estimate the mass to be accreted to the central object during the main accretion phase. The mass of the central object is the most essential as it makes it possible to determine the final mass of the central source when it is added to the mass to be accreted during its remaining main accretion phase.

The envelope mass is rather simply derived using continuum observations. However, estimating the accretion rate and the central mass is not trivial, requiring detailed observations of the outflow and disk structures, and suffers from many uncertain parameters and/or observational difficulties. For example, the two best candidates of the proto-BD are IC348-SMM2E (Palau et al. 2014) and L328-IRS (Lee et al. 2013). However, their identification as a proto-BD has yet to be concluded. IC348-SMM2E has been suggested to be a strong candidate of a proto-BD based on its low envelope mass ($\sim 0.03\,M_\odot$), small accretion rate ($\sim 1.6 \times 10^{-7}\,M_\odot\,\mathrm{yr}^{-1}$), and its low central mass ($\sim 0.02\,M_\odot$) from the Submillimeter Array (SMA) observations (Palau et al. 2014). However, their estimation of accretion rate was obtained by assuming an isothermal accretion process (Shu 1977) and has not yet been confirmed by observations. Moreover, the central mass was roughly inferred by assuming that the disk-like structure follows the Keplerian motions without any further detailed kinematical analysis of their SMA data.

There is a similar level of confidence regarding the BD status of L328-IRS. It has also been suggested to be a potential candidate of the proto-BD because it has small values for the envelope mass ($\sim 0.09\,M_\odot$), the accretion rate ($\sim 3.6 \times 10^{-7}\,M_\odot\,\mathrm{yr}^{-1}$), and the central mass ($\sim 0.05\,M_\odot$) (Lee et al. 2013). In this case, its envelope mass was fairly well determined from the continuum observations. However, the mass accretion rate was estimated from CO outflow observations with many uncertain parameters, especially the unknown inclination angle of the outflow. Moreover, the kinematical estimation of the central mass of this source was not

Table 1
Summary of Observing Parameters

Target	L328-IRS			
Continuum center coordinate	$(\alpha, \delta)_{J2000} = (18^h16^m59^s.4973 \pm 0.0002^s, -18°02'30''.263 \pm 0''.001)$			
Observing dates	2014 September 1		2015 April 14	
ALMA configuration	C34-6		C34-2	
Number of antenna	34		34	
Maximum baseline	1091.0 m		304.6 m	
Minimum baseline	40.6 m		14.1 m	
Bandpass calibrator	J1733-1304		J1733-1304	
Flux calibrator	Neptune		Neptune	
Gain calibrator	J1733-1304		J1733-1304	
Observations	Continuum	^{12}CO 2–1	^{13}CO 2–1	C^{18}O 2–1
Frequencies	231.5922 GHz	230.5380 GHz	220.3987 GHz	219.56036 GHz
Synthesized beam of combined data	$0''.31 \times 0''.23$(P.A. = $79°.3$)	$0''.33 \times 0''.25$(P.A. = $76°.9$)		
rms of combined data	$\sim$0.04 mJy beam^{-1}	$\sim$4.0 mJy beam^{-1} (0.096 km/s)$^{-1}$		

observationally possible because of the absence of spectral line observations in its possible disk region in high angular resolution. Instead, we estimated its total accreted mass and assumed it to be the mass of the central source.

In the recent ALMA era, however, it now becomes possible for us to look at very detailed outflow and disk structures at once in a protostellar or proto-BD system. This helps to constrain many parameters of these structures, and especially make a kinematical diagnosis of the disk rotation over the central object on a scale of a few tens of au to enable directly estimating the mass of the central object in its disk.

In this paper we present our ALMA observations of the L328-IRS region with subarcsecond angular resolution as well as a large recoverable scale of a few tens of arcseconds, aiming to identify an accreting disk in L328-IRS and constrain the detailed outflow structures, respectively. From this study we attempt to make a direct estimation of the mass of the central object as well as a more accurate calculation of the mass accretion rate in order to confirm whether L328-IRS belongs to the regime of a substellar mass.

L328-IRS was first identified in a dense core L328 as a Very Low Luminosity Object from observations by the *Spitzer* Space Telescope (Lee et al. 2009). Its bipolar outflows at the sub-pc scale were found from single dish observations (Lee et al. 2013). The mass accretion rate inferred from the outflow property was found to be smaller by almost one order of magnitude than the canonical accretion rate for low-mass protostars. Considering that its envelope mass is small, it has been suggested to be a strong precursor of the BD unless it has accreted enough mass in the past to evolve to a normal solar-type star. Because of inward motions found at the global scale over its envelope and some indication that L328-IRS is forming through a gravitational fragmentation process of the envelope, L328-IRS has been regarded as one of the best examples supporting the idea that a BD forms like a normal low-mass star (Lee et al. 2013).

In the next section we describe ALMA observations of L328-IRS in continuum and CO isotopolgue lines. Then we explain the results seen in the continuum and molecular line observations in Section 3. In Section 4, we discuss possible Keplerianity in the disk rotation and how the L328-IRS system would look in 3D space to help to reliably constrain an inclination angle of the outflow cavity from L328-IRS, the mass accretion rate, and the central mass of L328-IRS. We summarize our results in the last section.

2. Observations

L328-IRS was observed with ALMA in the ^{12}CO, ^{13}CO, and C^{18}O 2–1 lines, and 1.3 mm continuum during two observing dates in two different configurations of the Cycle 2 campaign (ALMA project number 2013.1.00783.S).

The first observation was made on 2014 September 1 in the C34-6 configuration with its maximum baseline of about 1091 m to achieve an angular resolution of $0''.33 \times 0''.25$ at 230 GHz. The second observation was carried out on 2015 April 14 in the C34-2 configuration. Its maximum baseline is about 305 m giving an angular resolution of $1''.43 \times 0''.78$, while its minimum baseline is about 14.1 m putting a limit of a maximum recoverable scale of $11''.4$. In both observations 34 (12 m) antennas were used.

We combined the data from two configuration observations in the visibility space and deconvolved the combined data to obtain the final image data. All the observing parameters are summarized in Table 1. We reduced our data with different robust weights, (1) natural, (2) uniform, (3) long baseline data only (baselines $>300k\lambda$), and (4) r (robust weight) = 0.5, to find any possible detailed structure in an angular resolution as high as possible. We found that the central disk-like emission is not bright enough to be useful for diagnosing its detailed kinematics with long baseline data only, for example, the robust weighted long baseline data (baselines $>300k\lambda$). Among the data that we tested with different robust weights, the data with $r = 0.5$ provided the most reasonable quality for our forthcoming analysis in terms of sensitivity and spatial resolution. The synthesized beam size of our combined data with $r = 0.5$ is $0''.31 \times 0''.23$ (P.A. = $79°.3$) in the continuum emission. The 1σ sensitivities for the continuum and line emission are measured to be $\sim$0.04 mJy beam^{-1} and $\sim$4.0 mJy beam^{-1} [0.096 km/s]$^{-1}$, respectively (Table 1).

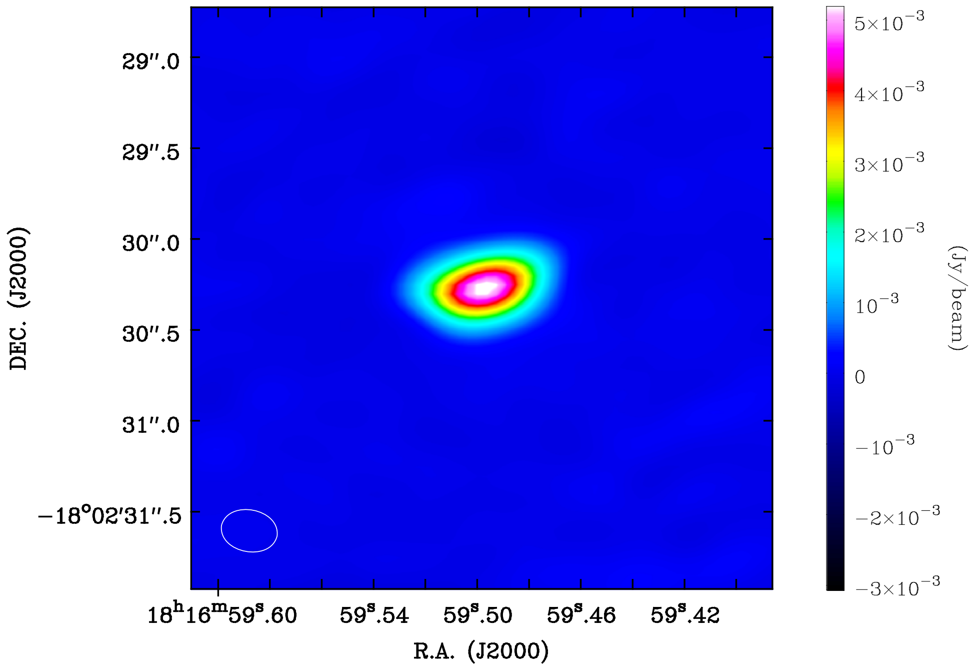

Figure 1. A single compact source showing a "disk-like" structure at the L328-IRS position in the 1.3 mm continuum emission. An open ellipse in the lower left corner is the synthesized beam of $0\rlap{.}''31 \times 0\rlap{.}''23$(P.A. = $79\rlap{.}^{\circ}3$).

3. Results

3.1. 1.3 mm Continuum

A single compact source of a "disk-like" structure at the L328-IRS position was detected in the 1.3 mm continuum emission within a primary beam field of view of $\sim 25\rlap{.}''2$ (Figure 1).

This continuum source was marginally resolved with the synthesized beam size. The image component size in the FWHM of the continuum is about $0\rlap{.}''54\,(\pm 0\rlap{.}''01) \times 0\rlap{.}''33$ $(\pm 0\rlap{.}''004)$ (P.A. $\sim 101\rlap{.}^{\circ}2 \pm 0\rlap{.}^{\circ}8$). Its FWHM size deconvolved by the beam is about $0\rlap{.}''40\,(\pm 0\rlap{.}''01) \times 0\rlap{.}''17$ $(\pm 0\rlap{.}''01)$ (P.A. $\sim 106\rlap{.}^{\circ}5 \pm 1\rlap{.}^{\circ}6$), which corresponds to $\sim$87 × 37 au in linear size at its distance ($\sim$217 pc, Maheswar et al. 2011). The peak position of the continuum is measured from its 2D Gaussian fit as $(\alpha,\ \delta)_{\mathrm{J2000}} = (18^{\mathrm{h}}16^{\mathrm{m}}59\rlap{.}^{\mathrm{s}}4973 \pm 0\rlap{.}^{\mathrm{s}}0002,\ -18^{\circ}\ 02'\ 30\rlap{.}''263 \pm 0\rlap{.}''001)$. The total integrated and peak intensities are estimated to be 11.40 (±0.22) mJy and 6.43 (±0.09) mJy beam^{-1}, respectively. We note that there is no other emission structure except for this disk-like compact emission in the field of view.

The mass for the continuum was calculated from

$$M_{\mathrm{cont}} = \frac{S_{1.3\mathrm{mm}} D^2}{B(T_{\mathrm{dust}})\kappa_{1.3\mathrm{mm}}}, \quad (1)$$

where $S_{1.3\ \mathrm{mm}}$ is the flux density at 1.3 mm, D is the distance of L328-IRS from us, $B(T_{\mathrm{dust}})$ is the Planck function at a dust temperature (T_{dust}), and $\kappa_{1.3\ \mathrm{mm}}$ is the dust opacity at 1.3 mm. If $\kappa_{1.3\ \mathrm{mm}}$ is assumed to be $\kappa_{\lambda} = 0.1 \times \left(\frac{0.3\ \mathrm{mm}}{\lambda}\right)^{\beta}$(Beckwith et al. 1990), then $\kappa_{1.3\ \mathrm{mm}}$ is given as $\kappa_{1.3\ \mathrm{mm}} = 0.014\ \mathrm{cm}^2\ \mathrm{g}^{-1}$ with $\beta = 1.3$ (Chandler & Sargent 1993). A gas to dust mass ratio is assumed to be 100 in converting the dust continuum mass into the total mass of the continuum source.

Our estimated total mass for the disk structure is about 0.01 $M_{\odot}$ at the dust temperature of 16 K from Lee et al. (2013) with a measured flux density of 11.4 mJy. However, note that the dust temperature of 16 K is the temperature for the dust envelope of about $\sim 20''$ ($\sim$4300 au) size surrounding L328-IRS and thus the temperature of the compact continuum source very near to L328-IRS can be higher. Thus, its likely mass may be smaller than 0.01 $M_{\odot}$ as estimated here. For example, if the temperature is assumed to be as high ($\sim$30 K) as that of B335 in smaller scale ($\sim$600 au) (e.g., Yen et al. 2015), the continuum mass would be as small as about 0.0045 $M_{\odot}$.

The most interesting feature in the continuum emission is its disk-like shape whose position coincides with the location of L328-IRS. We note that its position angle (P.A. $\sim 106\rlap{.}^{\circ}5 \pm 1\rlap{.}^{\circ}6$) is significantly different from that of the beam shape by about 27°, meaning that the disk-like shaped emission is not likely affected by the observed beam, but is instead a real feature.

3.2. CO Isotopologue Line Emission

3.2.1. Distribution of CO Emission

CO 2–1 line emission is known to well trace various kinematical structures of the molecular outflows in embedded YSOs (e.g., Bontemps et al. 1996). Previous single dish CO 2–1 observations by Lee et al. (2013) have shown that L328-IRS is producing CO outflows in a bipolar shape of the blue and red components at a sub-parsec scale. Our ALMA CO observations are found to well delineate the outflow part very near to L328-IRS in the range of $\sim$0–14.0 km s^{-1} in a manner consistent with the result obtained by the single dish observations, but with many more detailed structures of the compact outflow close to L328-IRS. Figure 2 shows the velocity channel maps of the CO emission, displaying various outflow-related structures near L328-IRS. One interesting structure that can be noticed is a rather high-velocity component seen only toward the central region of the disk-like continuum emission, probably emanating from L328-IRS.

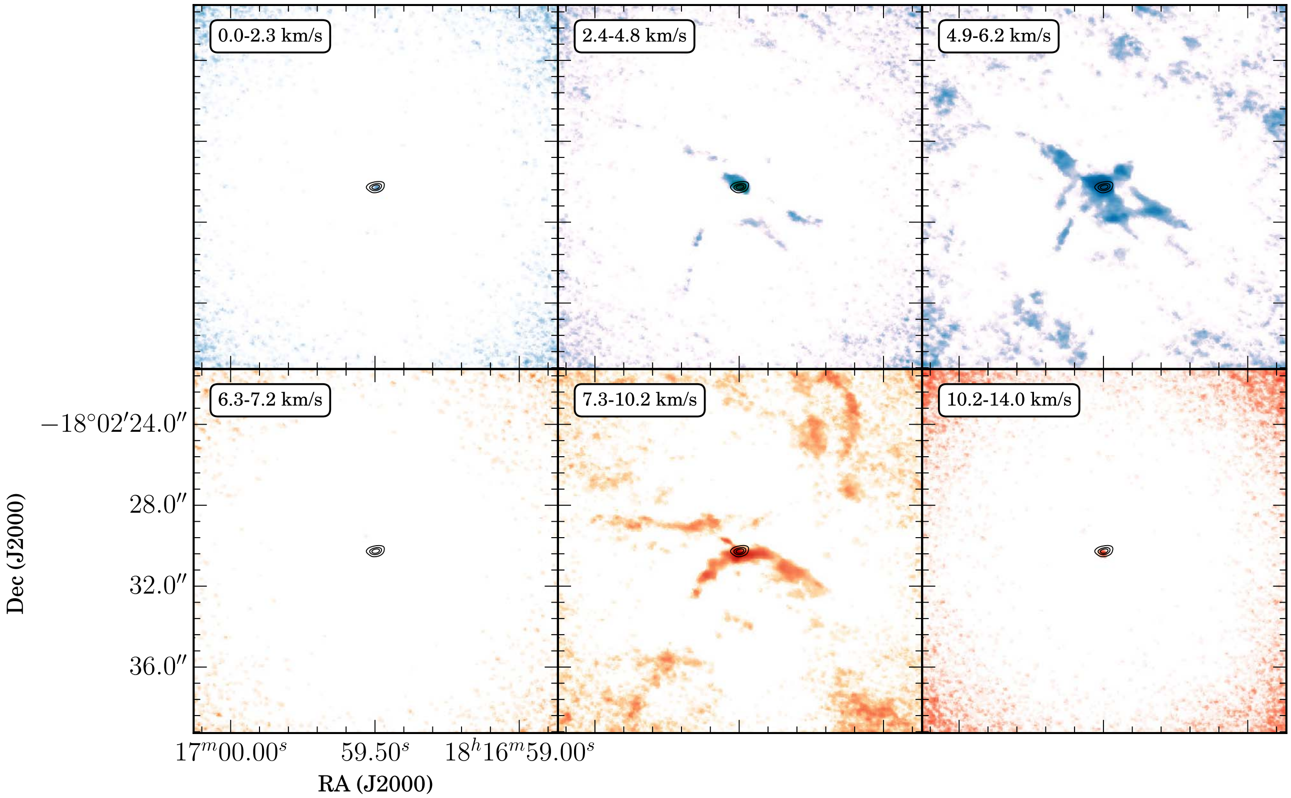

Figure 2. Velocity channel maps of the CO emission. In making the map the emission brighter than 18 mJy beam^{-1} [0.096 km s^{-1}]$^{-1}$ is considered. The disk-shaped continuum is drawn in contour levels, 1.1, 2.2, and 3.3 mJy beam^{-1}.

This is shown in both highly blue and redshifted ends at ∼0.0–2.3 km s^{-1} and ∼10.2–14.0 km s^{-1}, respectively. We believe that this may be a part of weak bipolar jets coming out from L328-IRS, projected to some degree to the line of sight.

The other noticeable feature is a blueshifted X-shaped structure in both the northern and southern regions, which is actually a typical feature of the bipolar outflow from a protostellar object. This structure appears at the velocity of ∼2.4 km s^{-1} and is seen up to ∼6.2 km s^{-1}. Then this is getting mixed with other structures, probably some parts of conic outflow shapes, including an arc structure in the southern region in the range of ∼4.9 to ∼6.2 km s^{-1}.

L328-IRS has a dense gas envelope of a few tens of arcseconds in size traced by dust continuum at 350 μm (Lee et al. 2009) or high-density molecular line tracers such as N_2H^+ 1–0 (Lee et al. 2013). The velocity range in the N_2H^+ line profile for this envelope identified by single dish observations is between ∼6.2 and 7.5 km s^{-1} as shown in Figure 2 of Lee et al. (2013). However, there is no emission at the similar velocity range in our ALMA data, between ∼6.3 and 7.2 km s^{-1}, and thus the absence of emission is thought to be most likely due to the envelope emission being resolved-out of the surrounding L328-IRS to be traced at relatively larger scale than the recoverable size (11.″4) in our observations.

The outflow components, which are now redshifted, appear again from the velocity of 7.3 km s^{-1}. The most striking features in the redshifted outflow are conic and arc shapes in the south and north directions, respectively. Southern conic outflow structures are seen between −7.3 and 8.8 km s^{-1} and the northern arc structure appears from about 7.5 km s^{-1} up to 10.2 km s^{-1}.

All these structures in the CO map are probably compressed parts of the bipolar outflow or just edges of the bipolar outflow where the column density becomes larger along the line of sight.

In Figure 3 we plot these various blues and redshifted outflow components seen as X, arc, and conic shapes in a single image with the dust continuum emission shown in the contour to help understand the overall structures of the outflow and the continuum emission. This figure now shows how blue and redshifted conic outflows in the southern lobes are well coincident with each other and how a blueshifted conic feature in the northern lobe is not well matched to a redshifted arc shape. We note that the continuum source is located on the tip of blue and redshifted lobes, and the long axis of the continuum emission (P.A. ∼ 106.°5) is almost perpendicular to the axis of the outflows (P.A. ∼ 11° as given in Section 4.2). This indicates that the continuum emission is likely a circumstellar disk for L328-IRS.

3.2.2. ^{13}CO Emission

^{13}CO line emission is not as bright as CO, and thus is seen only over the dense parts of the outflow close to the center of L328-IRS. This feature can be seen in its channel maps or the moment 1 map of the ^{13}CO emission in Figure 4. Blueshifted outflows appear at the velocity range of 4.6–6.1 km s^{-1}, while the redshifted outflows are seen at the velocity range of 7.0–8.0 km s^{-1}. The other velocity components at the velocities of 4.6–6.1 km s^{-1} and 8.0–9.3 km s^{-1} are distributed over the disk-like continuum structure and thus likely related to

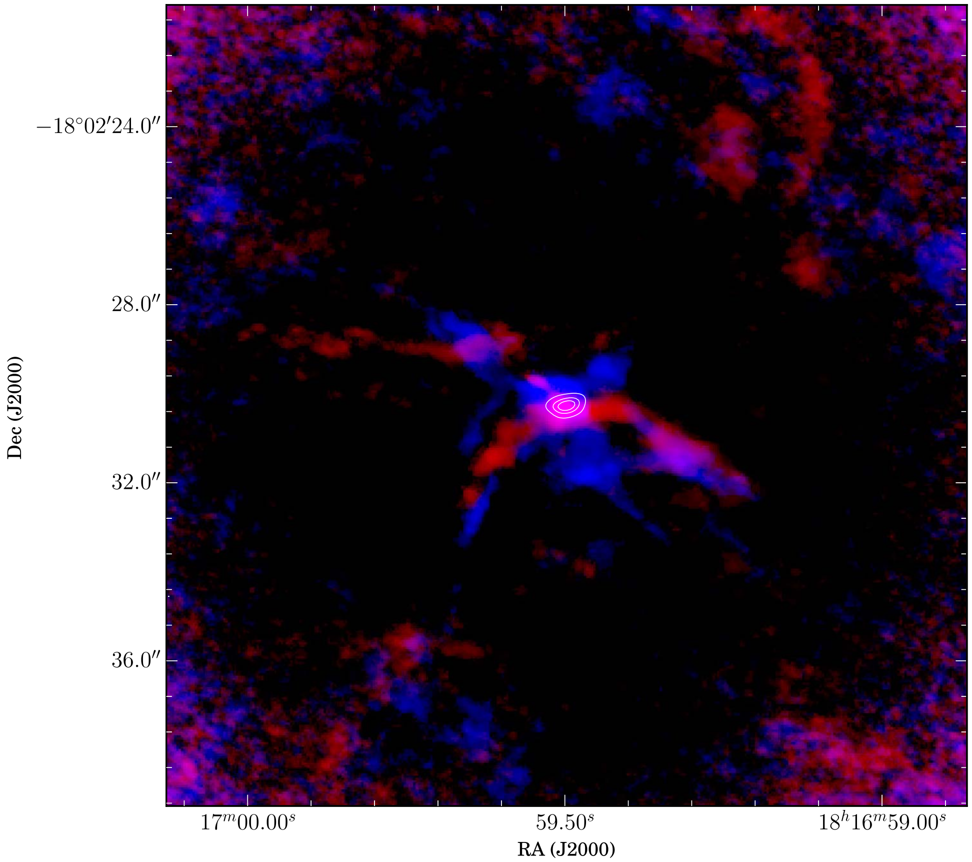

Figure 3. CO intensity map for blue and redshifted outflows in color tones with the dust continuum emission shown in the contours. In creating the map emission brighter than 15 mJy beam^{-1} [0.096 km s^{-1}]$^{-1}$ is considered. Contour levels for the dust continuum are the same as those in Figure 2.

rotational motions of disk-like components. Redshifted outflow component is also seen at 7.4–8.2 km s^{-1} along the direction of the major axis of the continuum emission. This is likely a dense part of redshifted CO outflow in a conic shape near the disk-like continuum emission as shown in Figures 2 and 3. It should be noted, however, that the moment 1 map actually shows some velocity gradient across the major axis of the disk-shaped continuum and thus ^{13}CO emission may be tracing some rotational motions in the structure of the disk-like continuum, while no such velocity gradient is seen in the CO emission map. So it seems that the ^{13}CO emission gives a velocity structure for the disk-like continuum, but at the same time the outflow activity near the disk-like structure makes it complicated to properly analyze the kinematics around the disk-like continuum. We will explain this further in the discussion section.

3.2.3. C^{18}O Emission

C^{18}O emission is known to be one of the best tracers for investigating the kinematics around the protostellar disks (e.g., Ohashi et al. 2014; Aso et al. 2017) and thus thought to be useful for examining the gas motions around the disk-like structure near L328-IRS. Figure 5 plots the moment 0 map of the C^{18}O emission with the dust continuum emission in the contour of its 5σ level ($\sim$0.2 mJy beam^{-1}), showing that overall C^{18}O emission traces the dust continuum region fairly well and the major axis of the CO emission distribution looks to be almost parallel to that of the continuum emission distribution in the NW-SE direction.

The overall kinematics near L328-IRS can be well examined by the moment 1 map of the C^{18}O emission shown in Figure 6. This figure clearly displays a velocity gradient along the direction of the elongated C^{18}O emission, which is very coincident with the major axis of the dust continuum emission drawn in a single contour of its intensity, while there is no clear velocity gradient along the short axis of the C^{18}O emission distribution. If the disk is rotating, the largest velocity gradient should be along the major axis, while there is no velocity gradient along the minor axis. These velocity features imply that a dominant kinematics in the disk-shaped C^{18}O emission may be a rotating motion. Therefore, the C^{18}O emission will be used in further analysis of the rotating kinematics in the disk structure of L328-IRS in the following section.

However, we should note that there are some complications that need to be considered in interpreting the rotational motions around L328-IRS using the C^{18}O emission. One complication may be due to the fact that the C^{18}O emission is not centrally peaked, but more likely flattened to the NW and SE directions, while the continuum emission is centrally peaked. We looked at C^{18}O spectra at the NW and SW parts of the disk, finding that the C^{18}O emission is significantly mixed with the other velocity components forbidden from the disk rotation. Such components can be also noticed in a position–velocity (PV) diagram along the major axis of the disk structure presented in the next section. Therefore, this flattened C^{18}O distribution to the NW and SE directions is thought to be mainly due to the existence of these forbidden components in those directions (in addition to the rotational components), which may be mostly outflow components coming out from L328-IRS. These

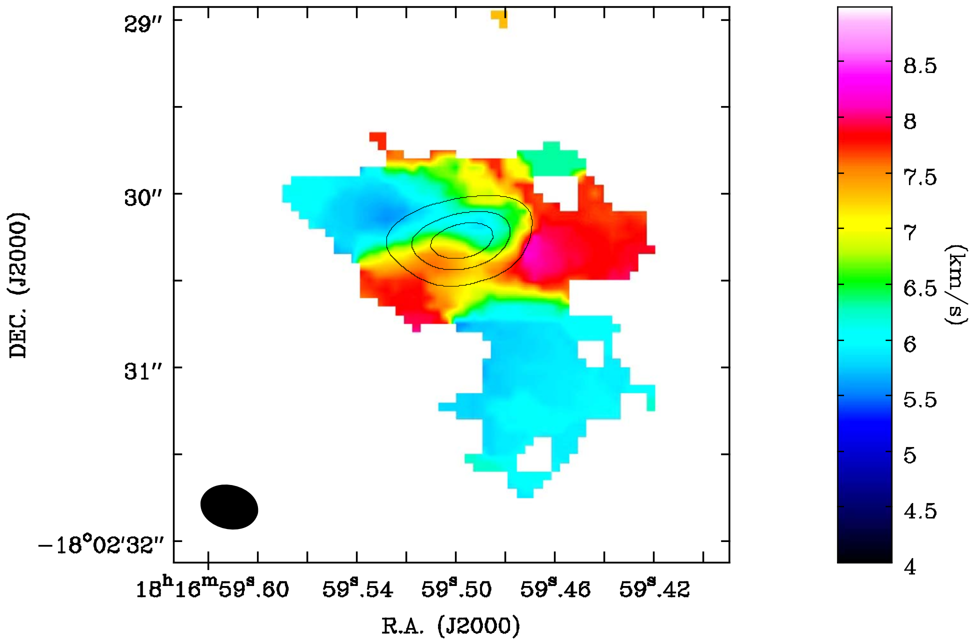

Figure 4. Moment 1 map of the ^{13}CO emission. The map shows the emission brighter than 2.2×10^{-2} mJy beam^{-1} [0.096 km s^{-1}]$^{-1}$, which is at the ~5σ level of the ^{13}CO emission. The dust continuum is overlaid at the same continuum levels as those in Figure 2.

forbidden components can be also seen in the moment 1 map of the C^{18}O emission in Figure 6 as the redshifted ones near the western edge of the disk structure.

The other complication may be due to the presence of C^{18}O components (mostly in the velocity range of 7.1–7.3 km s^{-1}) to the NE direction that are not seen in the disk-shaped continuum feature. Figure 6 indicates that these components may be some parts of the outflow emanating from L328-IRS toward the NE direction of the disk.

The third complication may be due to the fact that the direction (P.A. 36°.5) toward which there is no velocity gradient is slightly different from that (P.A. 16°.5) of the minor axis of the continuum disk, as shown in the moment 1 map of the C^{18}O emission. This is probably due to the presence of other motions such as outflows and/or infalling motions, which can disturb the rotational kinematics in the disk.

Therefore, in interpreting the kinematics of disk-like structure in the C^{18}O emission, it is important to consider that the C^{18}O disk of L328-IRS is not in purely rotational motions, but contaminated with these complex velocity components, which have nothing to do with the kinematics of the rotating disk structure.

The rotating and other kinematical features are also shown in the C^{18}O channel maps in Figure 7. The blueshifted components approaching us are clearly seen in the velocity range of 3.7–5.1 km s^{-1}, while the redshifted components moving away from us are seen in the velocity range of 8.7–10.3 km s^{-1}. We note that the faster blue or redshifted velocity components are at the inner disk part and the slower blue or redshifted velocity components are at the outer disk part, indicating that the disk may be in Keplerian rotation. However, we also note that some components in the range of 5.2–8.6 km s^{-1} are distributed well over the disk-like structure and likely regarded as other kinematical components like outflows and/or infalling structures, making the interpretation of disk kinematics more complicated. A more detailed analysis of the kinematics of the disk-like structure is given in the discussion section.

3.2.4. CO Isotopologue Line Profiles toward the Disk-like Continuum Structure of L328-IRS

A spectral line profile is another useful tool in diagnosing various kinematical features toward a protostellar object and its gas envelope. CO isotopologue lines are particularly useful to identify motions related to outflows, infall, and rotation toward protostars and their surrounding envelopes. Figure 8 plots CO isotopologue line profiles toward the most significant part of 1″.0 × 0″.6 of L328-IRS where the various gaseous motions such as the outflows, possible disk rotation, and infalling motions from its envelope may exist.

The CO 2–1 profile indeed shows a variety of interesting features. The line profile spans over a wide velocity range between 0 and ~14 km s^{-1} with absorption features in this range. By comparing the channel maps of the CO and C^{18}O emissions shown in Figures 2 and 7 with this CO profile, it is thought that most of the wide wing parts of the profile are the outflow components from L328-IRS, and the main bright profiles between about 3.0 and 6.2 km s^{-1} and 7.5 and 10.0 km s^{-1} are mostly the rotating disk component of L328-IRS. In addition, the CO profile shows a prominent absorption feature in the velocity range of ~6.2–7.5 km s^{-1}. As mentioned in the previous section, this absorption feature is due to the resolved-out phenomenon of the envelope emission surrounding L328-IRS at our ALMA observation, which has a very similar velocity span to that of the velocity range of the absorption profile. In the CO profile there is an even deeper absorption feature with negative intensity at ~7.4 km s^{-1}, the so-called inverse P Cygni profile. This is possibly due to an absorption of the disk continuum emission or resolved-out envelope emission by the redshifted "cool" foreground envelope gas, which is infalling toward L328-IRS. We suggest that the latter cause is more likely because such an absorption profile at similar velocity is also seen at various directions as

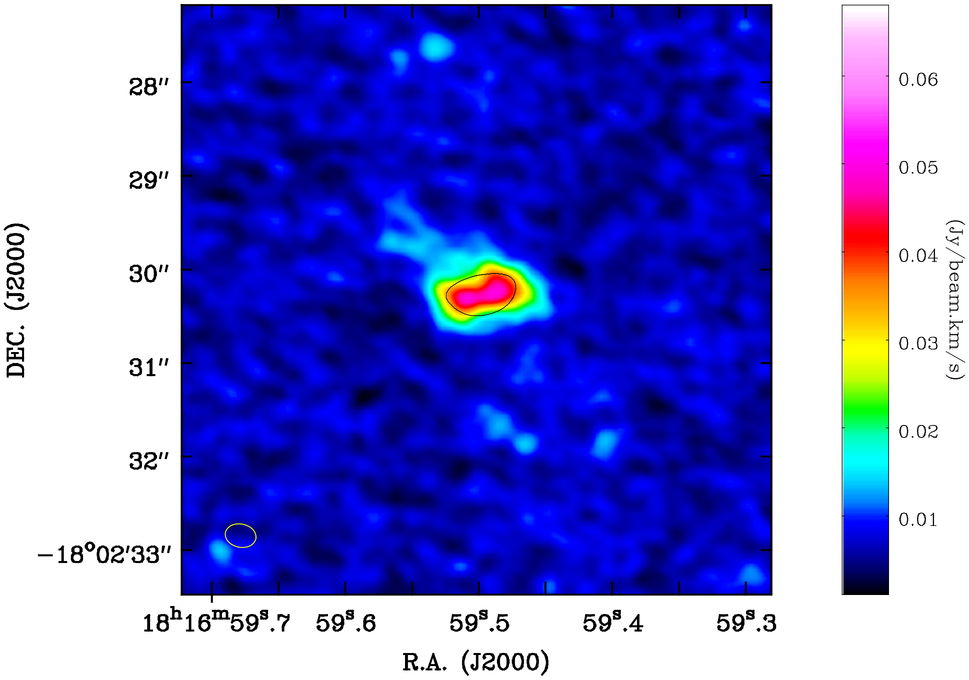

Figure 5. Moment 0 map of the $C^{18}O$ emission. The dust continuum emission is overlaid in a contour of ∼0.2 mJy $beam^{-1}$, which is at a 5σ level of intensity. In the map, at the 1σ level the $C^{18}O$ emission is about 5 mJy $beam^{-1}$ $[km\ s^{-1}]^{-1}$.

well as the direction of the central disk-like structure (Figure 9). It is noted that the absorption peak velocity of this profile is coincident with that (∼7.2 km s^{-1}) of the redshifted profiles (which may be redshifted infalling gas components) seen in infall asymmetric spectra of CO 3–2 and HCN 1–0 in the single dish observations (see Figure 2 of Lee et al. 2013).

If the systemic velocity is assumed to be 6.6 km s^{-1} as derived in the next section, then the infall speed will be roughly about 0.8 km s^{-1}. This inverse P Cygni profile is also seen in ^{13}CO and $C^{18}O$ lines, but to a somewhat different extent. In ^{13}CO the absorbed depth is shallower than that of the CO line and its absorption peaks at 7.2 km s^{-1}, which is slightly less redshifted. In $C^{18}O$ this absorption feature is weak, but enough to be recognizable, with its smallest redshift among the CO isotopologue lines. We will further discuss this profile and its implication in the next section.

The ^{13}CO 2–1 profile shows a similar feature to that of the main isotopologue line CO 2–1, but with some differences from the CO line profile. One main difference is that ^{13}CO 2–1 has narrower line wings than the CO line, covering the velocity range between ∼2.2 and 11.0 km s^{-1} where the emitting components are between ∼2.2 and 6.4 km s^{-1} and ∼7.4 and 11.0 km s^{-1}. This velocity coverage is still wide enough to see outflow emission at the farthermost velocity range from the systemic velocity, and the ^{13}CO emission near the systemic velocity is bright enough to investigate some of the kinematics of the innermost possible rotational motions of the disk-like emission structure. There is a feature of the inverse P Cygni profile that seems to be deep enough to infer infalling motions of gaseous material. The velocity range of the absorption feature due to the resolved-out foreground envelope emission is slightly smaller than that of the CO line.

The overall feature of the most rare isotoplogue $C^{18}O$ 2–1 profile appears to trace a similar velocity range to that by ^{13}CO 2–1, but the details are somewhat different from the ^{13}CO 2–1 line profile. For example, the velocity range of the $C^{18}O$ emission is slightly narrower than the ^{13}CO emission, covering ∼2.2–6.4 km s^{-1} and ∼7.1–10.5 km s^{-1}. Thus, the $C^{18}O$ emission may hardly trace outflow components at a higher velocity range than that of the ^{13}CO emission, and be less contaminated with other velocity components such as outflows. In fact, the $C^{18}O$ 2–1 line seems to well trace the central disk-like component without any significant contamination by other components such as the outflow. But it is weaker than ^{13}CO and thus may be less favorable in this regard in analyzing the kinematics of the disk component. In comparison, ^{13}CO shows stronger disk emission and thus can be better suited for investigating its kinematics than the $C^{18}O$ emission if other contaminating velocity components are properly extracted, when the $C^{18}O$ emission is too weak.

4. Discussion

4.1. Rotational Kinematics in the Disk and Its Implication

In the previous section we examined the kinematics in the disk-shaped structure seen in the dust continuum emission by using the moment 1 and the velocity channel maps of the $C^{18}O$ emission, suggesting that the disk may possibly be in Keplerian rotation, with some contamination of other kinematics such as infall and outflow motions. In this section we discuss whether the rotational motions in the disk-shaped structure follow a Keplerian kinematics or not and how the other motions can affect the rotating motions in the disk-shaped structure.

For this discussion we constructed a PV diagram (Figure 10) along the major axis (P.A. 106°.5) of the continuum disk in order to derive the rotational velocity of the disk emission as a function of the radius from L328-IRS. The linear distance of the emitting position from L328-IRS was estimated by assuming the distance of L328-IRS from the Sun to be ∼217 pc (Maheswar et al. 2011). In order to obtain the rotational velocity at each radius we made a cut profile along the velocity axis at each position in the PV diagram, which became a kind of intensity

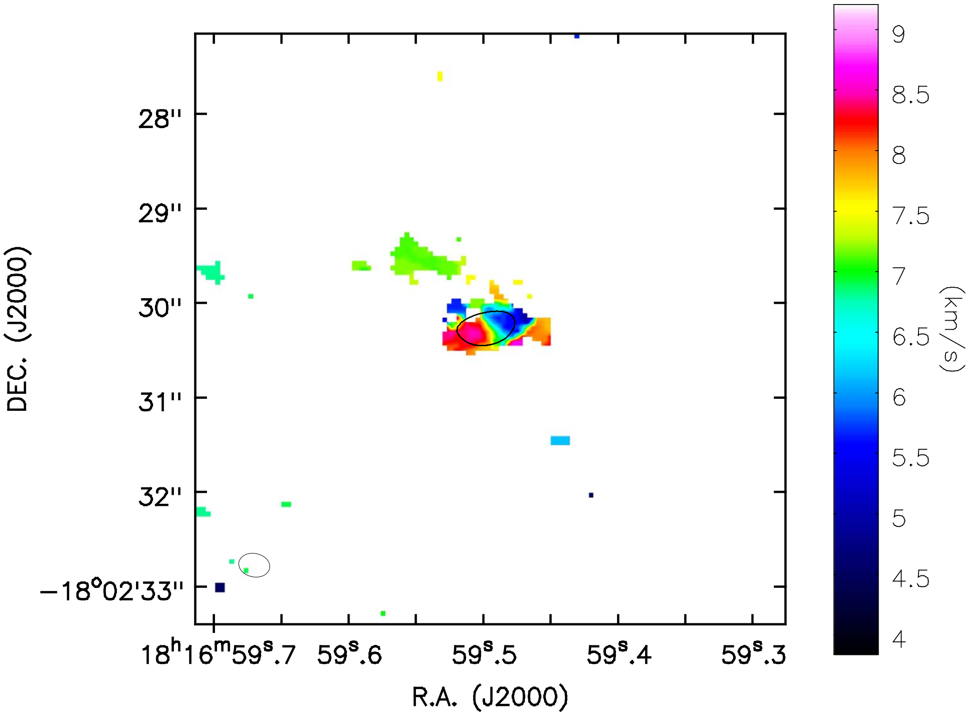

Figure 6. Moment 1 map of the $C^{18}O$ emission. The dust continuum emission is overlaid in the contour of its 5σ level (∼0.2 mJy beam^{-1}).

spectrum as a function of the LSR velocity at a given radius. We fitted each spectrum with a Gaussian function to obtain the velocity at its peak intensity at each position. As shown in the moment 1 map of $C^{18}O$, there are other kinematical contaminants in a disk rotation such as gas outflows or infalling motions. Some of those velocity components can be seen as forbidden in the rotational kinematics in the PV diagram. These are the components at the first and third quadrants in the left panels of Figures 10 and 11 and neglected in our analysis of the disk rotation. This way pure rotation components only could be extracted for the study of the rotational kinematics of the disk structure.

The Gaussian fit velocity was subtracted from the systemic velocity of the disk in order to obtain the projected rotational velocity of the disk. In this procedure the systemic velocity of the disk was determined to minimize the total summation of the differences between two Gaussian fit velocities in the blue and redshifted parts at the same radii of the disk from L328-IRS. Our obtained systemic velocity is 6.61 km s^{-1}, which is found to be very close to the systemic velocity value (∼6.7 km s^{-1}) of the envelope of L328-IRS obtained by a single dish observation (Lee et al. 2013). The rotation velocity was derived from the projected rotational velocity assuming that the disk is inclined at 25°.2 to the far direction of the sky plane, which is determined from $i = \arcsin\left(\frac{b}{a}\right)$ where a (=40″) and b (=17″) are semimajor and minor axes of the deconvolved disk. In estimating the inclination angle of the rotating disk of L328-IRS we assume that the disk is in a circular shape when it is viewed face-on and its observed shape is the one projected on the sky.

The constructed rotational velocity diagram for the gas motions along the major axis of the rotating disk is shown on the right-hand side of Figure 10. There, the rotational velocities (that are observationally derived) are plotted as a function of radius along the major axis of the disk-like structure with those for theoretical Keplerian motions in the disk by the central point sources of 0.05–0.4 $M_{\odot}$. A puzzling feature in Figure 10 is that the disk-like structure shows increasing velocities from a 130–60 au radius, while it has decreasing velocities from 60 au to the central region of the disk. We found that our data between 130 and 60 au are the best fitted with the Keplerian motions in the disk by a stellar object of ∼0.30 $M_{\odot}$. However, in contrast, the rotational velocity is not fitted with Keplerian motions at all toward the center of the disk from an ∼60 au radius. Its decreasing pattern within 60 au is close to that of solid rotation, although it is very unlikely that there is a solid rotation in the inner part of the gaseous disk.

We performed a similar analysis using the ^{13}CO line data. The ^{13}CO line emission is brighter than the $C^{18}O$ emission and thus may be more useful in the kinematical analysis of the faint disk emission in the $C^{18}O$ line. However, at the same time it may suffer more from the contamination by outflow motions. We made its PV diagram along the major axis of the disk emission and the rotation velocity versus disk radius diagram using the same procedures as described above for the $C^{18}O$ data (Figure 11). We found very similar results as can be seen in the diagrams of the $C^{18}O$ line data in Figure 10: Keplerian motions from a 140–60 au radius by a central object of ∼0.27 $M_{\odot}$ and decelerated motions from a 60 au radius to the central region of the disk.

At this moment it is hard to explain how the outer parts move like Keplerian motions, while the inner parts do not. One factor making the interpretation of the kinematics in the inner disk region difficult is that those parts are being affected by outflows and/or infalling motions. We did not include the gas components forbidden by the disk rotating motions as noted in this section, but it may be possible that our data still includes the components of the outflow or infalling motions at the disk parts very close to the central object, which seem to somehow follow the disk rotating direction, with a large departure from the rotating motions. In fact, Machida et al. (2009) showed

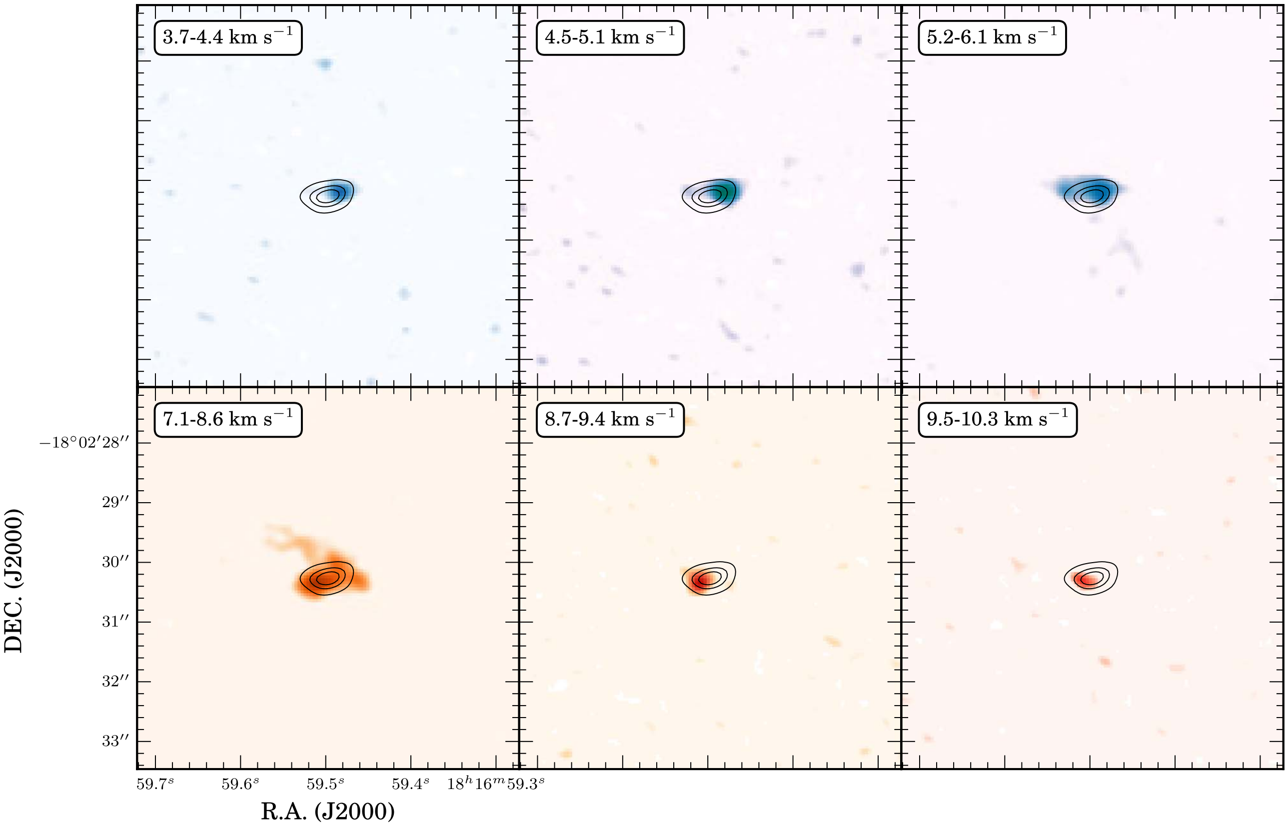

Figure 7. Velocity channel maps of the C^{18}O emission. The dust continuum is overlaid in contours at the same levels as those in Figure 2.

from their MHD simulation for the formation of a BD in a compact cloud core that these complicated motions can exist within a few tens of an au radius from the BD and thus can likely affect the interpretation of disk rotation motions if the observing lines do not trace the dense disk parts only.

There is the possibility that multiple unresolved sources in the inner disk region exist in the present observations and thus make tracing the kinematics within a few tens of an au radius more complicated.

Further study in the future with more appropriate line observations in better spatial resolution, which can better trace the rotational motions of the innermost parts without any contamination by other motions, may be extremely useful. For example, SO and H_2CO lines are found to be centrally enhanced in the protostellar disk and thus it may be useful to trace the inner kinematics in the disk (Ohashi et al. 2014; Sakai et al. 2014). With this kind of tracer in higher spatial resolution, better clarification of the gas kinematics in the disk structure of L328-IRS may be obtained in the near future.

4.2. Overall System of L328-IRS

All astronomical features are observed in projection on the sky to the line of sight. Thus, this always becomes an obstacle in correctly interpreting the physical characteristics of observed objects. However, this difficulty can be lessened or even overcome if the system has a symmetric shape and thus its 3D feature can be reasonably inferred.

Here we apply this idea for the L328-IRS system and discuss how this system having the infalling envelope, the outflows, and the disk, looks in three-dimensional space in order to attempt to draw a better inference of its whole structure and the related physical features. The key benefit of this process is to enable us to reliably infer the inclination angle of the outflow cavity, which is hardly known from single dish observations, and thus help to significantly reduce the main uncertain factor of the mass accretion rate.

The constructed 3D system of L328-IRS should be able to explain most of the observational characteristic structures shown in Figures 4 and 5, especially various outflow features such as X-shaped cavities, blue and redshifted arc structures seen in the south and north with respect to the disk structure, and inverse P Cygni profiles at various directions as well as the direction toward L328-IRS.

For this purpose we devised a simple toy model for L328-IRS. The model has the shape of the trapezoidal rotating body as shown in Figure 12(a) to mimic a simple shape of an outflow cavity. It consists of two cavities with a uniform thickness of 0.″45, which is assigned from the thickness of the X-shaped and arc structures seen in the CO map. The cavity structures have a spatial size of 15″ × 15″ consisting of 300 × 300 pixels^2, which is the same spatial size containing the same pixels^2 as our observing data. All the outflow emission is assumed to come from this thickened cavity structure only. It is also assumed in our simple toy model that all pixels in charge of the outflow structures emit the same intensity, there is no radiative transfer effect in the model system, and thus the line-of-sight intensity will be only the sum of the emission from the line-of-sight pixels.

In this simple model an exact velocity information could not be assigned for the model outflow structures. Instead, we could make a simple inclusion of at least blue or redshifted velocity information in the model outflow, by assigning a blueshifted velocity for the components at the nearer side from an observer

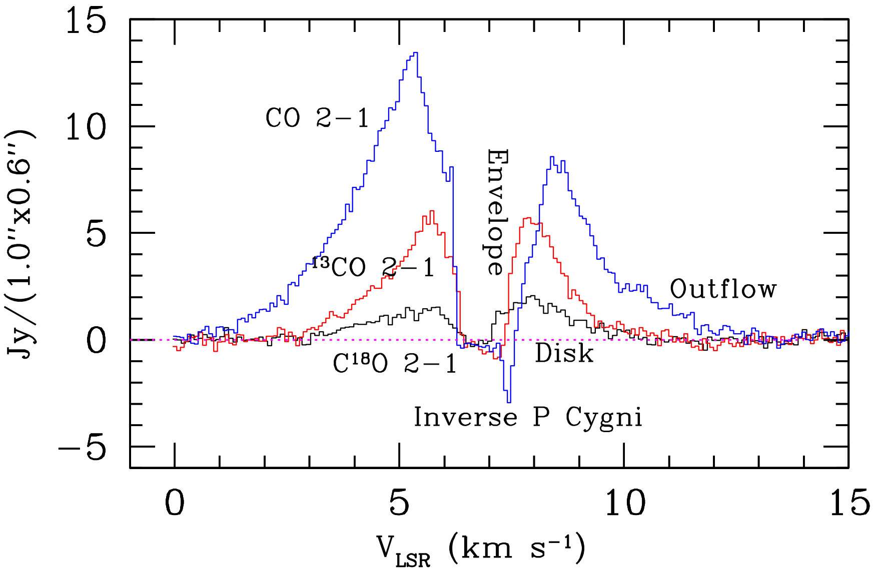

Figure 8. CO isotopologue line profiles integrated over the central area ($\sim1''.0 \times 0''.6$) of L328-IRS. These profiles show the signatures of various kinematical motions in this area, outflow, disk rotation, and infalling motions from envelope.

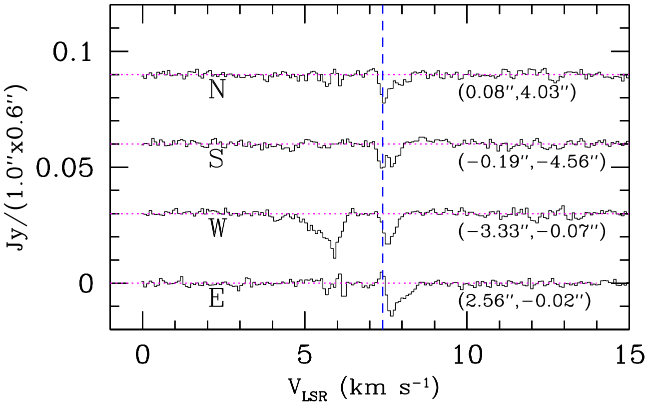

Figure 9. CO absorption profiles obtained (over the area of $1''.0 \times 0''.6$) in the four directions around L328-IRS. The directions N, S, W, and E, and offset values are relatively given with respect to L328-IRS. The dashed line indicates the position of the LSR velocity (∼7.4 km s^{-1}) for the absorption feature seen in the inverse P Cygni profile of CO in Figure 8. These absorption features seen in all the directions between ∼7.4 and 8.0 km s^{-1} are probably due to the absorption of the resolved-out background CO emission by the infalling cool gas in the foreground envelope.

with respect to the sky plane and a redshifted velocity for the other components at the farther side from the observer with respect to the sky plane as indicated in Figure 12(a).

Our observed data to compare with the model are composed of a blueshifted intensity map integrated between 2.24 and 6.24 km s^{-1} and a redshifted intensity map integrated between 7.78 and 10.4 km s^{-1}.

The simplest observational constraint we can make in the beginning for a search of the best model would be the position angle of the axis of the overall outflow structure, which turned out to be ∼11° from its observed shape.

The next parameters we can observationally constrain are the opening angle of the outflow cavity and the inclination angle of the outflow axis. Difficulty in constraining two parameters is that they are dependent on each other in a way that the projected value of the opening angle of the outflow cavity is highly affected by how the outflow axis is inclined. Thus, we examined the models with various inclination angles and opening angles in their wide parameters space to find the best model that can reproduce the observed intensity distribution of L328-IRS system.

The parameter space for the opening angle was examined between 75° and 105° around the likely value (90°) estimated from the observed X-shaped cavities. On the other hand, the best value of the inclination angle was searched between 50° and 80° because the most possible value would be around at 65°, which is estimated from the disk inclination.

The aspect ratio of the disk emission itself produces a degeneracy in inferring the inclination angle of the disk. In other words, the inclination angle can be either 65° or 115°. However, the blue and redshifted arc structures shown in Figures 4 and 5 can possibly be made only if the compressed or dense material exists in the redshifted northern cone and the blueshifted southern cone whose inclination (or the normal vector of the disk) is close to 65°. Therefore, we attempted to search for the best parameter for the inclination angle around 65°.

In this procedure one of the important observed features that we needed to reproduce was the arc structures seen in the northern and southern cones of the outflow cavity. We assumed that dense material exists in the arc shape in the cones, which is distributed in a separate structure in the northern and southern cones at the same distance from the center of the disk. The nearest distance of the arc structures from the center of the disk is given as $\sim1''.5$ as observed.

In searching for the best parameter set for the opening angle of the outflow cavity and its inclination angle we multiplied intensities from the same pixels between each model and the observed data, and summed them. This sum of the multiplied intensities between each model and the observed data is found to be a useful measure for examining the reproducibility of observing data by a model. The model giving the highest value will be the one that best reproduces the observation.

In the beginning we calculated the sum of the multiplied intensities between the observed data and 49 models at a 5° interval in the two searched parameter ranges to find a peak value of the sum of the multiplied intensities in the ranges of the opening angles of 85°–100° and the inclination angles of

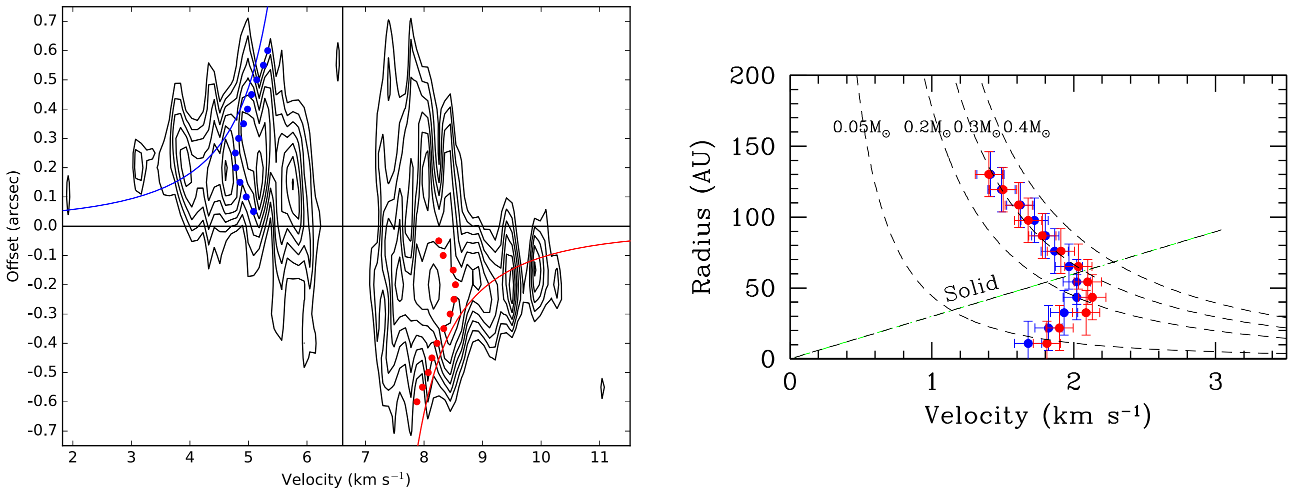

Figure 10. PV diagram of the C^{18}O emission in the disk (left panel) and its rotation velocity (right panel). The left panel shows a PV diagram of the C^{18}O emission along the major axis of the disk structure. The filled blue and red dots indicate the velocity points at the peak intensity obtained from the Gaussian fit to the cut profile along the velocity axis at each offset position. The blue and red curves are the trajectories that gases in the disk would rotate in Keplerian motions by a central object of ∼0.3 $M_\odot$. The right panel shows the rotational velocity as a function of the radius obtained using PV diagrams of the C^{18}O line data, indicating that the disk motions of L328-IRS are best fitted with Keplerian motions by a central object of ∼0.3 $M_\odot$ between 60 and 130 au in radius, while the motions within 60 au are not fitted at all with Keplerian motions.

65°–75°. Then we re-calculated the sum of multiplied intensities between observed the data and 256 models in a finer interval of 1° in these parameter ranges, finally finding that the peak value of the sum is produced at a model that has an opening angle of 92° and an inclination angle of 66°. Figure 12(b) shows this result in a relative ratio of the sum value of each model with respect to the sum value of the the best model, indicating that two parameters are very well constrained. This figure displays that a variation of 3°–5° for the opening angle and the inclination angle from the angle values of the best model outflow cavity will reduce ∼6% of the sum value at the peak.

The disk itself with a position angle of 106°.5 as measured in the previous section is rotating such that the eastern part is moving away from us while the western part of the disk is moving toward us. Therefore, we are probably seeing the bottom part of the disk, which is in counterclockwise rotation. We also notice that the disk is located on the bases of the outflow not in a symmetric center of the outflow bases such that western parts of the bases with respect to the center of the disk are longer than the eastern bases as mentioned above, implying that the eastern side of the disk are farther from us than the western part.

One promising kinematical feature shown in L328-IRS system is infalling motions in the gaseous envelope. In the previous section we showed inverse P Cygni profiles in the CO lines implying the existence of infalling motions of envelope gas material. These characteristic features are seen nearly all over the gas envelope of L328-IRS except for the regions where outflow activities are strong, with some variability of the negative intensities from region to region as shown in Figure 3. This indicates that infalling motions of gaseous material traced in CO 2–1 are occurring nearly all over the envelope of L328-IRS. Although this is not dealt within our simple toy model, we marked the infalling features in the model system shown in Figure 12(a). The overall schematic 3D view of L328-IRS system inferred from this work is depicted in Figure 12(a).

4.3. *ALMA Estimation of Mass Accretion Rate and Accretion Luminosity in L328-IRS, and Its Implication*

A mass accretion rate on a protostellar system is one of the most essential physical quantities to understand what the system would be and how it will evolve. Lee et al. (2013) have derived this rate for L328-IRS by using single dish data, concluding that L328-IRS has a very low-mass accretion rate (∼3.6 × 10^{-7} $M_\odot$ yr^{-1}), which is an order of magnitude less than the canonical value for a protostar (Shu et al. 1987; Dunham et al. 2006).

Here we re-estimate the mass accretion rate of L328-IRS with ALMA data. ALMA observations did not cover the whole area of the outflow, but they have an advantage in that the ALMA filters out large-scale envelope components and thus can preferentially trace compact outflow blobs. Therefore the ALMA data may provide a more accurate estimation of the physical quantities of the outflow with the least contamination by the envelope gas component. The mass accretion rate is estimated with the following equation formulated from the momentum conservation in a protostellar system under a process of the transformation of gravitational energy by the mass accretion to wind and/or jet energies (e.g., Bontemps et al. 1996):

$$\dot{M}_{\rm acc} = \frac{1}{f_{\rm ent}}\frac{\dot{M}_{\rm acc}}{\dot{M}_W}\frac{1}{V_W}F_{\rm outflow}, \tag{2}$$

where $f_{\rm ent}$ is an entrainment efficiency (<1), $\dot{M}_W$ is a wind/jet mass loss rate, V_W is a jet/wind velocity, and $F_{\rm outflow}$ is an outflow force. In this calculation we adopted the same values for $f_{\rm ent}(=0.25)$, $\frac{\dot{M}_W}{\dot{M}_{\rm acc}} = 0.1$, and the jet/wind velocity $V_{\rm W} \sim 150\,{\rm km\,s^{-1}}$ as those adopted by Lee et al. (2013) for the comparison. Here the outflow force $F_{\rm outflow}$ is given as

$$F_{\rm outflow} = \frac{\sum_i \sum_j P_{i,j}}{t_i}\frac{\sin\theta}{\cos^2\theta}, \tag{3}$$

where $P_{\rm i,j}$ is the outflow momentum $(=\sum_i \sum_j m_{i,j}(v_{i,j} - v_{\rm sys})$, where i and j are indexes for the summation over the positional

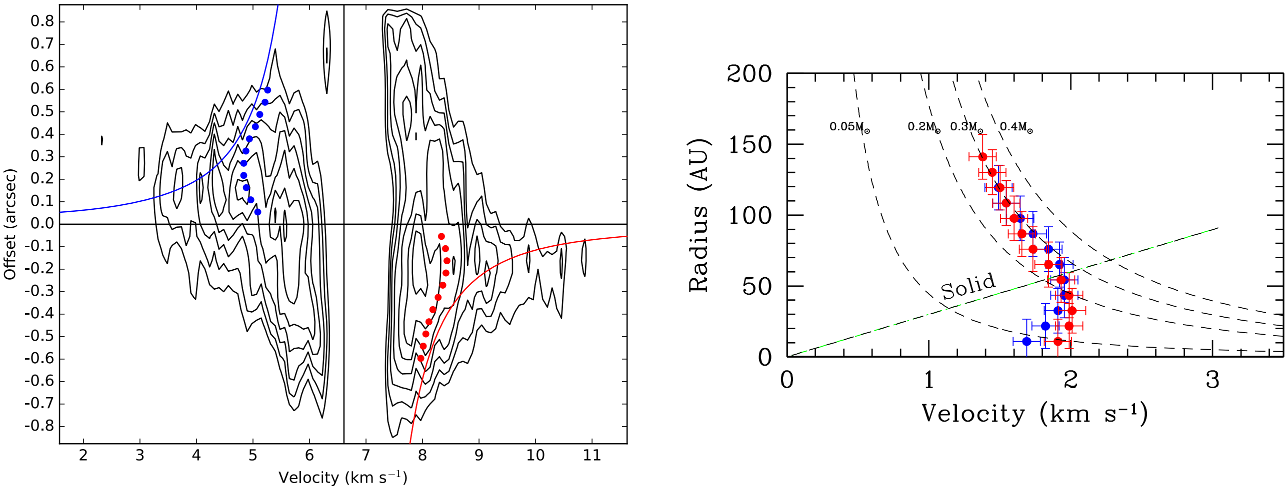

Figure 11. PV diagram of the ^{13}CO emission in the disk (left panel) and its rotation velocity (right panel). All markers in the diagrams have the same meaning as those in Figure 10, except that the ^{13}CO line data are being used. The data between 60 and 130 au in the radius in the diagrams are best fitted with Keplerian motions by a central object of $\sim 0.27\ M_\odot$, while the motions within 60 au are not fitted at all with Keplerian motions.

pixels and the velocity channels over the outflow, respectively.). Here t_i is a dynamical time of an outflow component at the ith pixel, the time over which an outflow blob at the ith pixel travels the distance (d_i) from L328-IRS to its position, given by

$$t_i = \frac{d_i}{|v_{i,j} - v_{\rm sys}|}\frac{\cos\theta}{\sin\theta}, \tag{4}$$

where $v_{i,j}$ is an LSR velocity of an outflow assigned by the jth velocity channel at the ith position pixel, $v_{\rm sys}$ is a systemic velocity of the L328-IRS system derived as 6.61 km s^{-1} in the previous section, and θ is an inclination angle of the outflow to the line of sight. The mass $m_{i,j}$ of the outflow blob with the jth velocity channel at the ith position pixel can be obtained by the column density multiplied by a pixel area of each position as follows:

$$m_{i,j} = \mu_{\rm H_2} m_{\rm H} N_{i,j} S_i, \tag{5}$$

where $\mu_{\rm H_2}$ is the mean molecular weight per hydrogen molecule ($\sim$2.8 for gas of a cosmic abundance of 71% hydrogen, 27% helium, and 2% metals by mass; Cox 2000), $m_{\rm H}$ is a mass of a hydrogen atom, $N_{i,\,j}$ is the column density of the outflow blob at the ith position pixel and jth velocity channel, and S_i is the ith pixel area. Here $N_{i,j}$ can be derived using CO 2–1 line observations by a following equation given for a transition of CO from a lower state J to an upper state $J+1$ with assumptions of a local thermodynamic equilibrium (LTE) condition and a thin optical depth toward the outflow blobs in the CO 2–1 profile (e.g., Dunham et al. 2014);

$$N_{i,j} = X_{\rm CO}\frac{3k}{8\pi^3\nu\mu^2}\frac{(2J+1)}{(J+1)}\frac{Q(T)}{g_j}e^{\frac{E_{J+1}}{kT}}T_{12}(i,j)\ \delta v\ [{\rm cm}^{-2}], \tag{6}$$

where $X_{\rm CO}$ is an abundance of CO relative to H$_2$ (assumed to be 10^{-4}, Frerking et al. 1982), k is the Boltzman constant, ν is the frequency for the CO 2–1 line (230.5380 GHz), μ is the dipole moment of CO (0.1098 Debye), $Q(T)$ is a partition function given by $Q(T) = \Sigma_{J=0}^{\infty} g_J e^{E_J/kT}$ at a temperature T, g_J is a degeneracy given by $2J+1$, T_{12} (i, j) is an intensity in K in the CO 2–1 line, and δv is a velocity channel width.

For the accurate calculation of the outflow force (or mass accretion rate) we attempted to reduce any possible uncertainties of the quantities given or implied in Equation (6). For example, Equation (6) is applicable only when the CO 2–1 line (even in its wing parts) is optically thin. However, CO 2–1 line profiles often get saturated (e.g., Arce & Goodman 2001; Curtis et al. 2010) and thus we need to make a proper correction on the high optical depth effect in the CO 2–1 line. For this correction C^{18}O 2–1 line data can be useful as the C^{18}O line has the least optical depth among the isotopologue lines that we observed. However, we used the ^{13}CO 2–1 emission because ^{13}CO 2–1 is detected fairly well over the outflow area around L328-IRS, while C^{18}O 2–1 is detected only over the disk area of L328-IRS. T_{12} $(i,\ j)$ can be opacity-corrected from the following equation under the assumption that the ^{12}CO and ^{13}CO are at LTE with the same excitation temperature and ^{13}CO 2–1 is optically thin:

$$T_{12}(i,j) = T_{13}(i,j)\frac{1-e^{-\tau_{12}(i,j)}}{\tau_{12}(i,j)}\frac{[^{12}{\rm CO}]}{[^{13}{\rm CO}]}, \tag{7}$$

where T_{13} $(i,\ j)$ is an intensity in K for the ^{13}CO 2–1 line, $\tau_{12}(i,j)$ is an optical depth of the CO 2–1 line at the ith position pixel and jth velocity channel, and $\frac{[^{12}{\rm CO}]}{[^{13}{\rm CO}]}$ is the abundance ratio, which is assumed to be 62 (Langer & Penzias 1993). In estimating the physical quantities we considered CO spectra brighter than 5σ. Our derived optical depths for CO were between 11 and 62.0 with mode values of 26.9 and 33.6 for the blue and red components, respectively, meaning that the CO 2–1 line emission is mostly optically thick.

This high optical depth in the CO 2–1 line led us to estimate excitation temperatures for the outflow blobs, which can also help to reduce the uncertainty in our calculation of the mass accretion rate. We estimated excitation temperatures for the outflow blobs to be about 9.9–38.2 K. We used these excitation temperatures and optical depths for the regions where ^{13}CO 2–1 is detected to derive the column density with better accuracy. However, for the regions where ^{13}CO 2–1 is not detected, we simply assume that the CO 2–1 line is optically

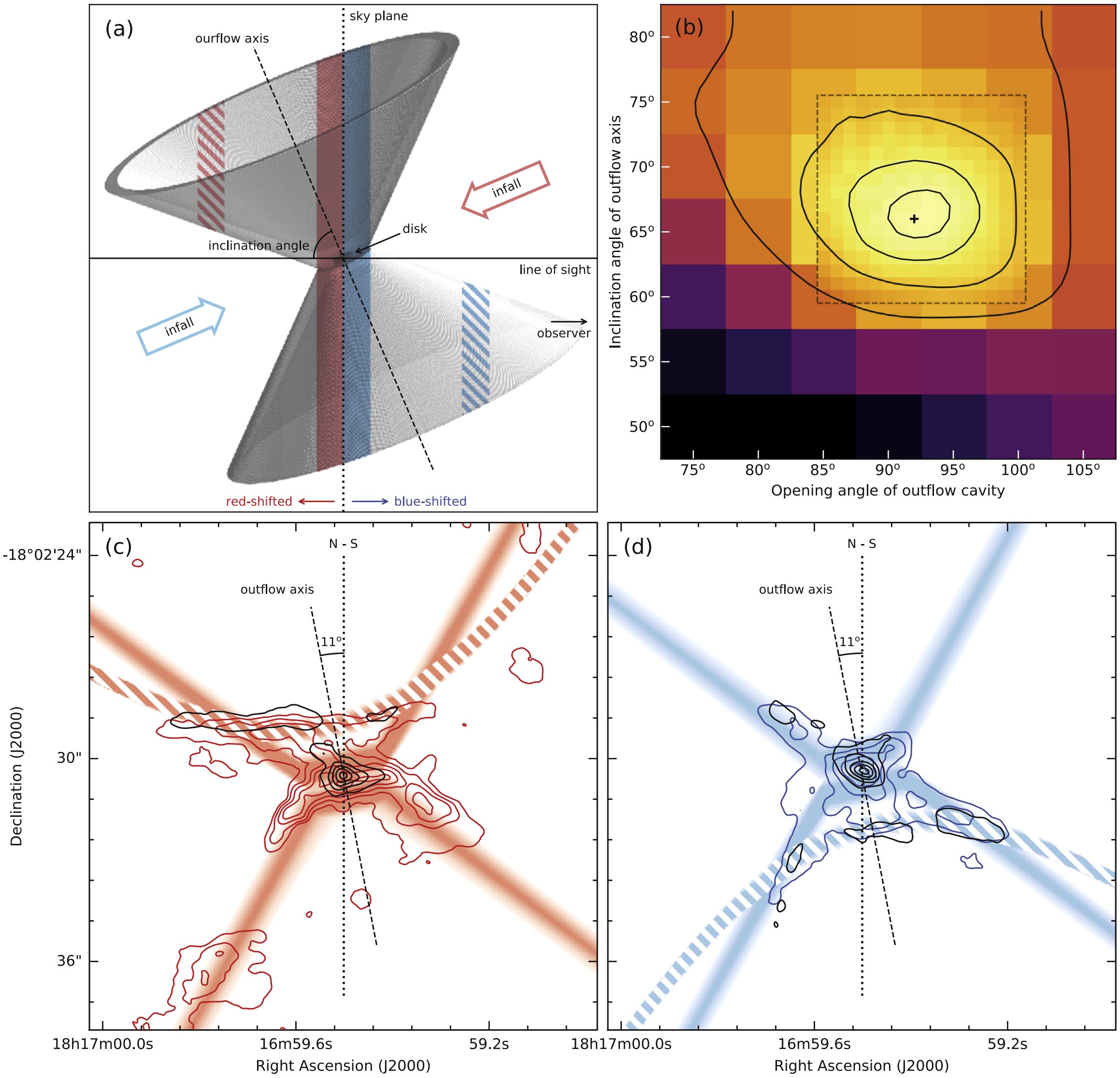

Figure 12. Possible 3D shape of the L328-IRS outflow system and comparison of its projected image with the observed image of the L328-IRS region. (a) Side view of our possible 3D model of the L328-IRS system. The observer is looking at L328-IRS from right to left. The dotted line from top to bottom indicates the sky plane. The conic structure has an opening angle of 92° and inclination angle of 66°, representing the shape of outflow cavities for L328-IRS. The simple velocity information for the conic outflows is implemented such that the components nearer to observer with respect to the sky plane is blueshifted and the components farther from the observer with respect to the sky plane is redshifted. The regions painted in blue and red tones and slanted lines in the outflow cavities are the parts used in reproducing the observed features in the intensity maps in (c) and (d). (b) Intensity reproducibility of the observed images with our model L328-IRS system in space with two parameters, the opening angle of the outflow cavity and the inclination angle of the outflow axis. The reproducibility is measured with a sum of the multiplied intensities between the observed data and each model. The figure shows the ratio for the sum value of each model with respect to the sum value of our best model with the opening angle of 92° and inclination angle of 66°. The ratio is expressed with the color tones or contours in this panel. This was calculated at 5° intervals outside the dashed box and at 1° intervals inside the dashed box. The cross symbol indicates the point of the highest reproducibility, and contours are drawn at levels of 98%, 94%, 86%, and 70% with respect to the cross point. (c) Comparison of the redshifted images (shown in contours) for the observed L328-IRS system with those (drawn in red and slanted lines) of our model L328-IRS system. Two overlaid contours in red and black contours are to show the integrated intensities between $\sim$7.28 and 8.24 km s^{-1} and $\sim$8.32 and 10.40 km s^{-1}, respectively. (d) Comparison of the blueshifted images (shown in contours) for the observed L328-IRS system with those (drawn in blue and slanted lines) of our model L328-IRS system. Two overlaid contours in blue and black contours are to show the integrated intensities between $\sim$5.28 and 6.24 km s^{-1} and $\sim$2.24 and 5.20 km s^{-1}, respectively. The projected images on the sky of this 3D configuration model of the L328-IRS system can mostly explain well the observed features in detail.

thin and the excitation temperature is as cold as $\sim$9.9 K, and calculate the column density using Equation (6). Choosing the other value for the excitation temperature is found to be not sensitive to the final result for the mass accretion rate because the outflow force at the central region of L328-IRS where the excitation temperature is properly determined is dominantly high (two orders of magnitude higher than any other regions where the excitation temperature cannot be determined). For example, our estimation with the excitation temperature of 38.2 K for the regions where ^{13}CO 2–1 is not detected gives almost the same total outflow force and mass accretion rate as the results with the excitation temperature of 9.9 K.

Our analysis of L328-IRS images with the 3D toy model also helps to make a better determination of the mass accretion rate because some of parameters for the outflow structures in 3D are well constrained and thus can be used in the calculation of the mass accretion rate with much less uncertainties. For example, an inclination angle of the outflow is usually poorly known.

Table 2
Summary of Our Estimation of the Mass of L328-IRS

Method	Estimated Mass	Notes
Dynamical mass	$\sim 0.3\,M_\odot$	Inner disk not fully fitted with Keplerian motion
Mass inferred from $L_{\rm int}$	$\sim 0.012\,M_\odot$	Valid only if $L_{\rm int}$ is due to $\dot{M}_{\rm acc}$
Mass accreted during dynamical time	$\sim 0.023\,M_\odot$	Valid only if $\dot{M}_{\rm acc}$ is constant during dynamical time

However, our analysis gives a well constrained value of ~66° as explained in the previous section, reducing the uncertainty in the estimation of the mass accretion rate.

In this way we estimate the outflow forces of all the outflow blobs, from which a total mass accretion rate is derived to be $\sim 8.9 \times 10^{-7}\,M_\odot\,{\rm yr}^{-1}$. Our previous value (with an inclination angle of $\sim 57\overset{\circ}{.}3$) from the single dish observations is $\sim 3.6 \times 10^{-7}\,M_\odot\,{\rm yr}^{-1}$, which corresponds to a value of $\sim 6.9 \times 10^{-7}\,M_\odot\,{\rm yr}^{-1}$ at the outflow inclination angle of ~66°, indicating that our new estimation of the mass accretion rate with ALMA data is consistent with the value obtained from the single dish observations.

With this mass accretion rate and the mass M_* of the central source, the accretion luminosity of L328-IRS can be derived by using the equation $\frac{GM_*\dot{M}_{\rm acc}}{2R}$, if this luminosity is mostly due to accretion from the disk to the central object L328-IRS (e.g., Baraffe et al. 2009), where G is the gravitational constant and R is the radius of the central object. If the disk rotation is purely in Keplerian motions by the mass of L328-IRS of $\sim 0.3\,M_\odot$, its accretion luminosity is estimated to be $\sim 1.3\,L_\odot$, which is more than one order of magnitude brighter than its internal luminosity $\sim 0.05\,L_\odot$ (Lee et al. 2009) that stands for the present accretion luminosity. So far there is no clear evidence yet for the episodic accretion in the L328-IRS system and thus the accretion process may have been made likely in a quiescent manner until the present. Then the mass of L328-IRS may be overestimated by more than one order of magnitude.

If the internal luminosity is due to our estimated accretion rate in a quiescent manner, the mass of L328-IRS to produce its internal luminosity of $\sim 0.05\,L_\odot$ can be estimated to be $\sim 0.012\,M_\odot$ (rather than $\sim 0.3\,M_\odot$). Provided that only a limited amount (about 20%–40%, Lada et al. 2007; André et al. 2010) of the envelope mass ($\sim 0.1\,M_\odot$) can accrete onto the central object, L328-IRS would have the final mass of a BD.

There is an alternative way to infer the likely mass of L328-IRS, which is to estimate its accreted mass. The accreted mass may be the first order approximate value of the central mass of L328-IRS because most of the mass accretion toward the proto-BD may occur at the very early stage and then the initially high mass accretion rate can rapidly (and highly) decrease by 10^2–10^6 times in a very short time of 10^4 years since the formation of the substellar object (Machida et al. 2009). L328-IRS is believed to have its outflow activity at least during the dynamical timescale of $\sim 6.4 \times 10^4 \frac{\cos\theta}{\sin\theta} \approx 2.8 \times 10^4$ years (at the outflow inclination angle of ~66°) from Lee et al. (2013) so that most of the central mass may have already been accreted. Therefore, the total accreted mass would be $\sim 0.023\,M_\odot$ in this case with an assumption of 10% extraction of the accreted mass through the outflow (Pelletier & Pudritz 1992; Bontemps et al. 1996). This value well matches to the mass that we estimated from the assumption that the internal luminosity for L328-IRS is mainly due to the accretion process in L328-IRS, and is again in the regime of substellar mass. Table 2 summarizes the methods we used to infer the mass of L328-IRS and their related problems.

In conclusion, these rough methods for inferring the central mass of the L328-IRS system seem to suggest that our estimate of the central mass does not exceed the mass of a BD. However, we should emphasize that L328-IRS can have a stellar mass to produce its accretion luminosity equivalent to the internal luminosity if it is currently acquiring mass in a much smaller $\dot{M}_{\rm acc}$ at least by an order of magnitude than the past. Therefore, we cannot completely rule out the possibility that L328-IRS can have a stellar mass, too. We also note that our estimation can be subject to uncertainties. Our estimation of the accretion rate can be affected by various uncertain parameters, including the entrainment efficiency, the ratio of mass accretion rate to a wind/jet loss rate, jet/wind velocity, and other parameters involved in the estimation of blob mass. Moreover, the mass accretion rate may have varied during the outflow activity of L328-IRS, and the accretion rate during the rest of the Class 0 phase is quite uncertain (e.g., Machida et al. 2009; Machida & Hosokawa 2013) so that the assumption of our constant accretion rate in the total estimation of the accreted mass may not be valid. In any case, a dynamically direct estimation of the central mass by looking for the Keplerian motions in the inner disk region with future ALMA observations in the right tracers may be helpful in making a more concrete identification of L328-IRS.

5. Summary

In this paper we presented our observing results on the central region of L328-IRS with a 1.3 mm continuum at ALMA band 6 and the ^{12}CO, ^{13}CO, and C^{18}O 2–1 lines. Although L328-IRS has been known to be a proto-BD candidate because of its small mass accretion rate (a few $10^{-7}\,M_\odot\,{\rm yr}^{-1}$) and small envelope mass of $\sim 0.09\,M_\odot$, its identity as a substellar object has not been confirmed because its central mass has never been directly determined. In this study we attempted to precisely measure the central mass of L328-IRS as well as its mass accretion rate by using these ALMA observations in order to help to confirm whether L328-IRS is in a regime of a substellar object. Our results are summarized as follows;

1. We found a disk-like structure in continuum whose deconvolved size is about $0\overset{''}{.}40 \times 0\overset{''}{.}17$ (~87 au × 37 au). This structure is believed to be a rotating disk around L328-IRS in the sense that its major axis is almost perpendicular to the outflow axis and its moment 1 maps in the ^{13}CO and C^{18}O 2–1 lines do not show any clear velocity gradient along the minor axis of the disk structure, but a significant velocity gradient along its major axis. We investigated whether the rotational motions follow Keplerian kinematics, finding that the motions are only partially fitted with a Keplerian motion between 130 and 60 au by a central object of $\sim 0.30\,M_\odot$, but not for the inner region of $\leqslant$60 au radius. With the

mass of ∼0.3 $M_\odot$, the accretion luminosity of L328-IRS is estimated to be ∼1.3 $L_\odot$, which is much brighter than its known internal luminosity ∼0.05 $L_\odot$, making us believe that the disk is not likely in Keplerian motions and the central mass of L328-IRS cannot be kinematically determined from this study yet.

2. Our ALMA data provide detailed bipolar outflow structures emanating from L328-IRS, helping us to better define the outflow parameters and thus derive the mass accretion rate with better accuracy. For this process we constructed a 3D toy model of L328-IRS, consisting of an outflow cavity of the rotating trapezoidal shape whose spatial size and pixels are given the same as those of our ALMA data. All pixels in this simple model were assumed to emit the same intensity without a radiative transfer effect in the model system so that the line-of-sight intensity is the sum of emission from the line-of-sight pixels. The red or blue-shifted velocity information is simply given with respect to the plane of the sky in order to compare its projected structures with our key outflow structures seen in CO observations such as the X-shaped outflows and the arc-like structures in the cones.

   From this comparison our observed features of the outflow were found to be best reproduced if the outflow had an inclination angle of ∼66° and an opening angle of ∼92°. The additional correction for the high optical depth for the CO outflow and the estimation of the excitation temperature for the CO outflow as well as precise constraining of the inclination angle of the outflow led us to estimate a more reliable value of the mass accretion rate, which is $\sim 8.9 \times 10^{-7}\,M_\odot\,\mathrm{yr}^{-1}$. This new estimation is found to be fairly consistent with the value derived previously from the single dish observations.
3. By using the newly derived mass accretion rate, we inferred the central mass of L328-IRS in two indirect ways. One is to assume that the internal luminosity is due to this accretion rate in a quiescent manner. Then the central mass of L328-IRS to reproduce its internal luminosity is estimated to be ∼0.012 $M_\odot$. The other way is to estimate the mass accreted during the dynamical timescale of $\sim 2.8 \times 10^4$ years, assuming a constant accretion rate. This gives a total accreted mass of ∼0.023 $M_\odot$. Our indirect ways imply that the central mass of L328-IRS is likely in the regime of substellar mass.

However, we cannot rule out the other possibility that L328-IRS has a stellar mass if its current mass accretion rate is much smaller than the average value during its outflow activity. Moreover, these methods are subject to various uncertainties, especially regarding the mass accretion rate. Thus, the identification of L328-IRS as a proto-BD must be considered tentative. Future direct kinematical measurement of the central mass with more appropriate ALMA observations is needed to clarify the identity of L328-IRS.

We thank an anonymous referee for a thorough reading of our manuscript and giving us very useful comments with which our paper was significantly improved. This research was supported by Basic Science Research Program through the National Research Foundation of Korea (NRF) funded by the Ministry of Education, Science and Technology (NRF-2016R1A2B4012593).

This paper makes use of the following ALMA data: ADS/JAO.ALMA#2013.1.00783.S. ALMA is a partnership of ESO (representing its member states), NSF (USA), and NINS (Japan), together with NRC (Canada), MOST, and ASIAA (Taiwan), and KASI (Republic of Korea), in cooperation with the Republic of Chile. The Joint ALMA Observatory is operated by ESO, AUI/NRAO, and NAOJ.

ORCID iDs

Chang Won Lee https://orcid.org/0000-0002-3179-6334
Gwanjeong Kim https://orcid.org/0000-0003-2011-8172
Philip C. Myers https://orcid.org/0000-0002-2885-1806
Masao Saito https://orcid.org/0000-0003-0769-8627
Woojin Kwon https://orcid.org/0000-0003-4022-4132
A-Ran Lyo https://orcid.org/0000-0002-9907-8427
Archana Soam https://orcid.org/0000-0002-6386-2906
Mi-Ryang Kim https://orcid.org/0000-0002-1408-7747

References

André, P., Men'shchikov, A., Bontemps, S., et al. 2010, A&A, 518, L102
Arce, H., & Goodman, A. A. 2001, ApJ, 554, 132
Aso, Y., Ohashi, N., Aikawa, Y., et al. 2017, ApJ, 849, 56
Baraffe, I., Chabrier, G., & Gallardo, J. 2009, ApJ, 702, 27
Basu, S., & Vorobyov, E. I. 2012, ApJ, 750, 30
Bate, M. R. 2009, MNRAS, 392, 590
Bate, M. R. 2012, MNRAS, 419, 3115
Beckwith, S. V. W., Sargent, A. I., Chini, R. S., & Guesten, R. 1990, AJ, 999, 924
Bonnell, I. A., Clark, P., & Bate, M. R. 2008, MNRAS, 389, 1556
Bontemps, S., Ward-Thompson, D., & André, P. 1996, A&A, 314, 477
Boss, A. P. 2001, ApJL, 551, L167
Chandler, C. J., & Sargent, A. I. 1993, ApJ, 414, 29
Cox, A. N. (ed.) 2000, Allen's Astrophysical Quantities (4th ed.; New York: AIP Press, Springer), 28
Curtis, E. I., Richer, J. S., Swift, J. J., & Williams, J. P. 2010, MNRAS, 408, 1516
Dunham, M. M., Arce, H. G., Mardones, D., et al. 2014, ApJ, 783, 29
Dunham, M. M., Evans, N. J., II, Bourke, T. L., et al. 2006, ApJ, 651, 945
Frerking, M. A., Langer, W. D., & Wilson, R. W. 1982, ApJ, 262, 590
Lada, C., Alves, J. F., & Lombardiet, M. 2007, in Protostars and Planets V, ed. B. Reipurth, D. Jewitt, & K. Keil (Tucson, AZ: Univ. Arizona Press), 3
Langer, W. D., & Penzias, A. A. 1993, ApJ, 408, 539
Lee, C. W., Bourke, T. L., Myers, P. C., et al. 2009, ApJ, 693, 1290
Lee, C. W., Kim, M.-R., Kim, G., et al. 2013, ApJ, 777, 50
Luhman, K. L. 2012, ARAA, 50, 65
Machida, M. N., & Hosokawa, T. , 2013, MNRAS, 431, 1719
Machida, M. N., Inutsuka, S., & Matsumoto, T. 2009, ApJ, 704, 10
Maheswar, G., Lee, C. W., & Dib, S. 2011, A&A, 536, A99
Ohashi, N., Kazuya, S., Yusuke, A., et al. 2014, ApJ, 796, 131
Padoan, P., & Nordlund, A. 2004, ApJ, 617, 559
Palau, A., Zapata, L. A., Rodrguez, L. F., et al. 2014, MNRAS, 444, 833
Pelletier, G., & Pudritz, R. E. 1992, ApJ, 394, 117
Reipurth, B., & Clarke, C. 2001, AJ, 122, 432
Sakai, N., Oya, Y., Sakai, T., et al. 2014, ApJ, 791, 38
Shu, F. H. 1977, ApJ, 214, 488
Shu, F. H., Adams, F. C., & Lizano, S. 1987, ARA&A, 25, 23
Whitworth, A. P., & Zinnecker, H. 2004, A&A, 427, 299
Yen, H.-W., Takakuwa, S., & Koch, P. M. 2015, ApJ, 812, 129